Aalto University

Giani, Stefano; Hakula, Harri

On effects of perforated domains on parameter-dependent free vibration

On effects of perforated domains on parameter-dependent free vibration

Stefano Giani [a], Harri Hakula [b],*

[a] Durham University, School of Engineering and Computing Sciences, South Road, Durham, DH1 3LE, United Kingdom
[b] Aalto University, Department of Mathematics and System Analysis, P.O. Box 11100, FI 00076 Aalto, Finland

A R T I C L E   I N F O

A B S T R A C T

Free vibration characteristics of thin perforated shells of revolution vary depending not only on the dimensionless thickness of the shell but also on the perforation structure. All holes are assumed to be free, that is, without any kinematical constraints. For a given configuration there exists a critical value of the dimensionless thickness below which homogenisation fails, since the modes do not have corresponding counterparts in the non-perforated reference shell. For a regular $g \times g$-perforation pattern, the critical thickness is reached when the lowest mode has an angular wave number of $g/2$. This observation is supported both by geometric arguments and numerical experiments. The numerical experiments have been computed in 2D with high-order finite element method supporting Pitkäranta's mathematical shell model.

1. Introduction

Solving partial differential equations (PDEs) over complicated domains remains a challenge even with modern computing environments. In this work we are interested in parameter-dependent eigenproblems on one specific class of complicated domains, namely the perforated ones. Ultimately one would hope to use homogenisation techniques for instance to find effective material parameters in elasticity problems. What makes parameter-dependent eigenproblems interesting in this context is that the eigenmodes can be modelled as dynamical systems. It is possible that the perforations lead to perturbations in the spectrum including mixing of modes. In such a situation it is not sufficient just to know the reference configuration, but also be able to match the modes between the reference and perturbed configurations. In other words, relying on the order of modes can lead to physically incompatible matchings.

Our model application is a linear elasticity one of engineering interest — the free vibration of perforated thin shells of revolution. The introduction of both Martikka et al. [1] and Kalamkarov et al. [2] provides an excellent overview for various related applications. Our initial interest to this particular problem is from homogenisation of effective material parameters in this context, in particular Jhung and Yu [3]. There exists a substantial body of literature on related problems, where the material used in the construction has some structure of its own, for instance, composites with varying properties in the thickness direction, see [4–6].

The central parameter is the dimensionless thickness of the shell, t. We assume that the shell has a constant thickness d, which is replaced in the dimension reduction by $t = d/L$, where L represents some characteristic length scale, typically the diameter of the computational domain. For different types of shell geometries the asymptotic behaviour for both the smallest eigenvalues and related modes are known as the thickness of the shell tends to zero. For references in the

* Corresponding author.
   E-mail addresses: stefano.giani@durham.ac.uk (S. Giani), Harri.Hakula@aalto.fi (H. Hakula).
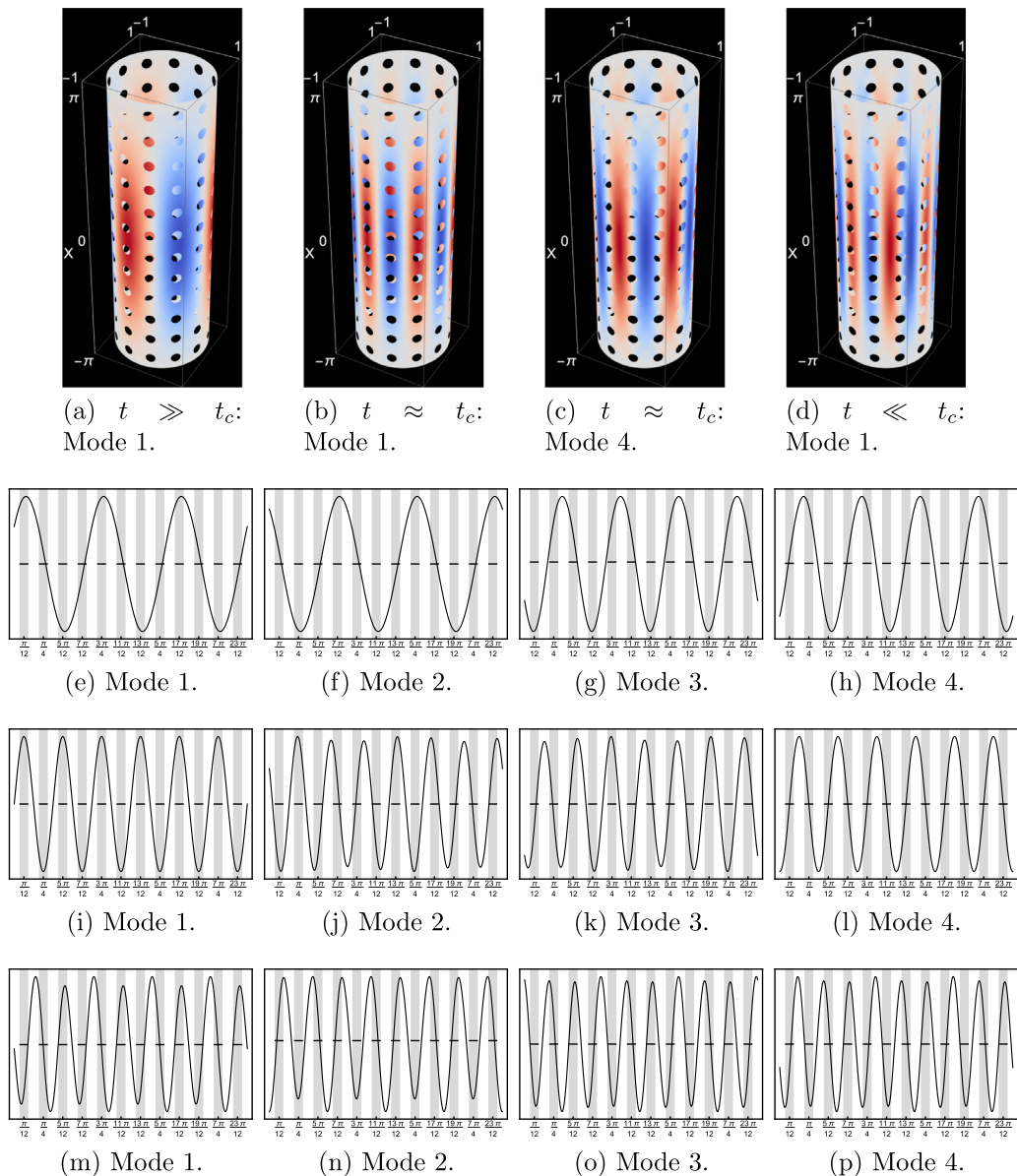
Fig. 1. Transverse deflection profiles of the smallest eigenmodes on 12 × 12 regular grid with hole coverage percentage of 12%. The ends are clamped, but the holes are free. Illustration of the global and local feature ranges: top row, surface plots, second row, $t = 1/100 \gg t_c$, third row, $t = 0.007 \approx t_c$, and bottom row $t = 0.0025 \ll t_c$. On the top row, notice the alignment with respect to the perforation pattern of the Modes 1 and 4 at $t \approx t_c$. Profiles plotted along the middle line ($x = 0$) avoiding any perforations; locations of the perforation rows are marked with horizontal lines and light grey background. In the third row the wave numbers of the 1st and 4th modes are the same.

style used here, see for instance [7–11]. At least for the cylindrical shells, the dynamics of the eigenmodes are now well understood. For this class of structures, clusters of eigenmodes arise naturally due to symmetries. It follows that clusters can be identified with mode-dependent quantities of interest, such as the wave number of the mode in the angular direction.

One of the main results of this paper is that there is a connection between the perforation patterns and the dimensionless thickness. For every structured pattern there exists a *critical thickness* or parameter value t_c, below which the dynamics have a different asymptotic behaviour. The approximate critical value of t_c can be predicted with high reliability using the theoretical *a priori* information available, once the given configuration is related to a reference one. Based on the characteristics of the smallest eigenmode, the parameter range $t \in [t_0, t_1]$ can be divided into two parts: the *global feature* range with $t_1 \geq t \geq t_c$, where the mode has the same features as in the reference case, and the *local feature* range with $t_0 \leq t \leq t_c$, where the asymptotic behaviour does not follow the reference case and the local features due to the perforation pattern begin to affect the mode. In Fig. 1 the transverse deflection profiles of the smallest eigenmodes on

12×12 regular grid with hole coverage percentage of 12% at three different parameter values are shown. The values of t have been chosen to illustrate qualitatively the transition of the modes around the critical value. Of particular interest is the row of profiles starting from Fig. 1i. Notice that the modes belong to two clusters, with Modes 1 and 4, and 2 and 3, being the basis modes of the respective clusters. The Modes 1 and 4 have the same wave numbers, but the separation within the cluster comes from the maximal amplitudes coinciding with the perforations in Mode 1, and the minimal ones with the perforations in Mode 4. This observation is central to our analysis.

In engineering applications the perforation patterns are hardly ever random, since there is an underlying assumption of repeatability in designs. Therefore we do not consider fully random perforations but deterministic patterns derived from quasi-Monte Carlo quadrature rules. The numerical experiments indicate that the value of the critical thickness depends on the average density of the perforations, however, the sharpness of the value depends on the quality of the pattern with the strongest effect with regular perforation patterns.

It is interesting to contrast these results with those in the context of perforated shells under static loading. There a similar phenomenon of dominant local features is observed, but the source of the local features is the excitation of both boundary and internal layers at the boundaries of the perforations and within the patterns. Such localisation in eigenmodes occurs only at high in the spectrum, however. The shapes or wave numbers of the smallest modes we are focusing on are driven only by the internal layers.

The rest of the papers is structured as follows: In Section 2 we introduce the shell model, including the perforations, and outline the *hp*-finite element method (FEM) used in the numerical experiments. The asymptotics of the modes and their dynamics with the clusters are the topics of Sections 3 and 4, respectively. The numerical experiments (Section 5) are followed by concluding remarks in Section 6.

2. Preliminaries

In this section we cover the model problem, discuss perforation patterns including the quasi-Monte Carlo ones based on Halton sequences, and finally give a brief overview of the *hp*-FEM used in our numerical experiments below. As always with preliminaries, most of the material is available in many previous studies. However, since the focus in this paper is more on the parameter-dependent effects rather than shell problems as engineering problems, the shell model presented next is highly simplified and suitable for relative easy implementation within any FEM-solver framework.

2.1. Model problem: Parabolic shell of revolution

As our model shell geometry we choose the cylinder − the simplest parabolic shell. We start by introducing the connection between the exact shell geometry and the curvature tensor central to the mathematical shell model. We start by defining the shell geometry first and then outline the shell model used in the numerical experiments.

2.1.1. Shell geometry

In this work we study thin shells of revolution. They can formally be characterised as domains in $\mathbb{R}^3$ of type

$$\Omega = \{\mathbf{x} + z\mathbf{n}(\mathbf{x}) \mid \mathbf{x} \in \omega, -d/2 < z < d/2\}, \tag{1}$$

where d is the (constant) thickness of the shell, ω is a (mid)surface of revolution, and $\mathbf{n}(\mathbf{x})$ is the unit normal to ω. For realistic geometries we assume principal curvature coordinates, where only four parameters, the radii of principal curvature R_1, R_2, and the so-called Lamé parameters, A_1, A_2, which relate coordinate changes to arc lengths, are needed to specify the curvature and the metric on ω. There are other options, however. We can simplify the model above by assuming that ω can be unfolded as a rectangular domain expressed in the coordinates x_1 and x_2. We denote this computational domain with D (Fig. 2). Furthermore, we assume that the curvature tensor $\{b_{ij}\}$ of the midsurface is constant, and as already mentioned in the introduction, in the sequel we replace the thickness d with the dimensionless thickness $t = d/L$, where $L \sim \text{diam}(D)$.

Let us consider a cylindrical shell generated by a function $f_1(x_1) = 1$, $x_1 \in [-x_0, x_0]$, $x_0 > 0$. In this case the product of the Lamé parameters (metric), $A_1(x_1)A_2(x_1) = 1$, and the reciprocal curvature radii are $1/R_1(x_1) = 0$ and $1/R_2(x_1) = 1$, since

$$A_1(x_1) = \sqrt{1 + [f_1'(x_1)]^2}, \quad A_2(x_1) = f_1(x_1), \tag{2}$$

and

$$R_1(x_1) = -\frac{A_1(x_1)^3}{f''(x_1)}, \quad R_2(x_1) = A_1(x_1)A_2(x_1). \tag{3}$$

Thus, in the simplified model we can choose $b_{11} = 0$, $b_{22} = 1$, and $b_{12} = b_{21} = 0$, and arrive at a very good approximation of the exact geometry.

(a) $f_1(x_1) = 1,\ x_1 \in [-\pi, \pi]$.

(b) $D = [-\pi, \pi] \times [0, 2\pi]$
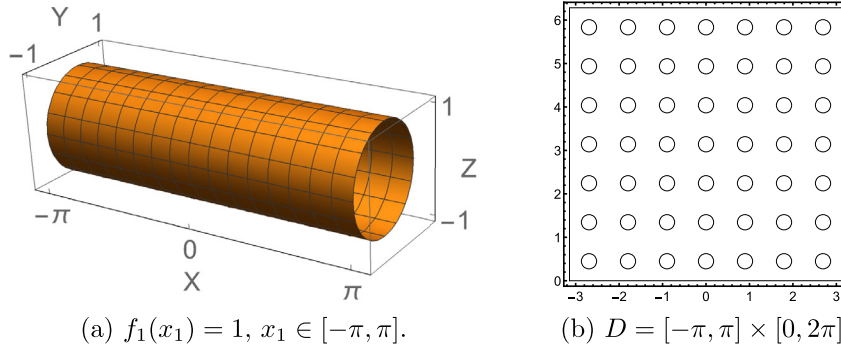
Fig. 2. Parabolic shell of revolution and the corresponding computational domain with a 7 × 7 regular perforation pattern with 12% hole coverage. For free vibration the boundaries at $x_1 = \pm\pi$ are clamped, holes are free, and $x_2 = 0$ and $x_2 = 2\pi$ are periodic.

2.1.2. Two-dimensional mathematical shell model

Our two-dimensional shell model is of the so-called Reissner–Naghdi type [12] − the mathematical shell model by Pitkäranta [13], where the transverse deflections are approximated with low-order polynomials. The resulting vector field has five components $\mathbf{u} = (u, v, w, \theta, \psi)$, where the first three are the displacements and the latter two are the rotations in the axial and angular directions, respectively. Here we adopt the convention that the computational domain D is given by the surface parametrisation and the axial/angular coordinates are denoted by x and y.

Deformation energy $\mathbf{A}(\mathbf{u}, \mathbf{u})$ is divided into bending, membrane, and shear energies, denoted by subscripts B, M, and S, respectively.

$$\mathbf{A}(\mathbf{u}, \mathbf{u}) = t^2 \mathbf{A}_B(\mathbf{u}, \mathbf{u}) + \mathbf{A}_M(\mathbf{u}, \mathbf{u}) + \mathbf{A}_S(\mathbf{u}, \mathbf{u}). \tag{4}$$

Bending, membrane, and shear energies are given as

$$t^2 \mathbf{A}_B(\mathbf{u}, \mathbf{u}) = t^2 \int_D \left[\nu(\kappa_{11}(\mathbf{u}) + \kappa_{22}(\mathbf{u}))^2 + (1-\nu) \sum_{i,j=1}^{2} \kappa_{ij}(\mathbf{u})^2 \right] dx\, dy, \tag{5}$$

$$\mathbf{A}_M(\mathbf{u}, \mathbf{u}) = 12 \int_D \left[\nu(\beta_{11}(\mathbf{u}) + \beta_{22}(\mathbf{u}))^2 + (1-\nu) \sum_{i,j=1}^{2} \beta_{ij}(\mathbf{u})^2 \right] dx\, dy, \tag{6}$$

$$\mathbf{A}_S(\mathbf{u}, \mathbf{u}) = 6(1-\nu) \int_D \left[(\rho_1(\mathbf{u})^2 + \rho_2(\mathbf{u})^2 \right] dx\, dy, \tag{7}$$

where ν is the Poisson ratio (constant). We have omitted the scaling $E/(12(1-\nu^2))$, where E is the Young's modulus. The strains are (with the curvature tensor values already inserted) as follows:

$$
\begin{aligned}
\kappa_{11} &= \frac{\partial \theta}{\partial x}, \quad \kappa_{22} = \frac{\partial \psi}{\partial y}, \quad \kappa_{12} = \frac{1}{2}\left(\frac{\partial \theta}{\partial y} + \frac{\partial \psi}{\partial x} \right), \\
\beta_{11} &= \frac{\partial u}{\partial x}, \quad \beta_{22} = \frac{\partial v}{\partial y} + w, \quad \beta_{12} = \frac{1}{2}\left(\frac{\partial u}{\partial y} + \frac{\partial v}{\partial x} \right), \\
\rho_1 &= \frac{\partial w}{\partial x} - \theta, \quad \rho_2 = \frac{\partial w}{\partial y} - \psi.
\end{aligned}
\tag{8}
$$

2.2. Perforation domains

Perforated domains are characterised by the penetration patterns which in turn depend on the underlying manufacturing processes and the related hole coverage, typically given as a percentage. Here we consider standard structured patterns and extend the concepts to quasi-random patterns. We also consider a simple randomised damage model.

2.2.1. Regular penetration patterns

The quantity used to characterise perforated sheets of metal is the ligament efficiency η. Let us assume that the holes are ellipses with a, b as the horizontal and the perpendicular semiaxis, and the separation of the centres is P_x and P_y, respectively. Following [3,14,15], we define the horizontal and the perpendicular ligament efficiency, denoting them as η_x, η_y, respectively. For regular arrays of holes

$$\eta_x = (P_x - 2\,a)/P_x, \qquad \eta_y = (P_y - 2\,b)/P_y, \tag{9}$$
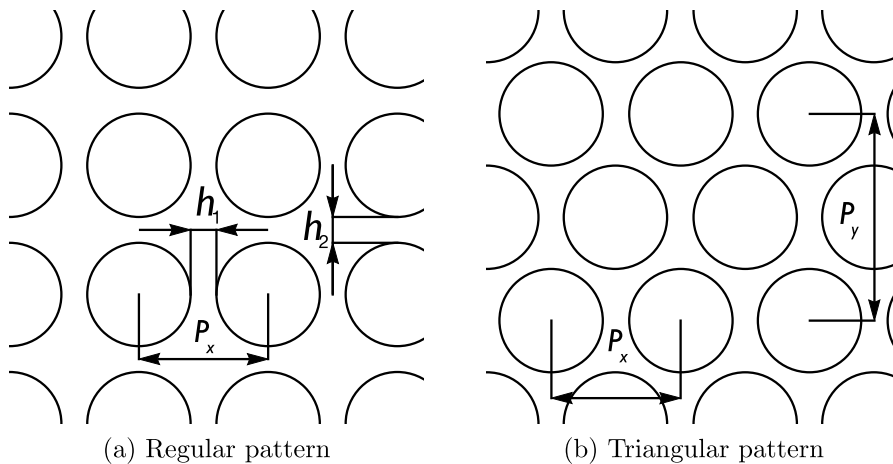
(a) Regular pattern　　　　　(b) Triangular pattern

Fig. 3. Penetration patterns.

and for triangular arrays, allowing for alternating layers,

$$\eta_x = (P_x - 4\,a)/P_x, \qquad \eta_y = (P_y - 4\,b)/P_y. \tag{10}$$

For circular holes the radius $r = a = b$, of course, and further if the pattern is regular $\eta = \eta_x = \eta_y$. Both pattern types are illustrated in Fig. 3. Notice that the triangular pattern in the figure has a tighter packing than that implied by (10).

2.2.2. Quasi Monte-Carlo

An intriguing option is to replace a regular pattern with one induced by a quasi-random process. Notice that quasi-random means that the process is deterministic which has implications to manufacturing. Of course, the ligament efficiencies cannot be defined as above. One of the simplest sequences of points generated by such a process is the Halton sequence [16].

Definition 1 (*Halton*)**.** Let $i \in \mathbb{N}_0$ and basis $b \in \mathbb{N}$ be such that $b \geq 2$. Then the inverse representation function $\phi_b(i)$ is given by

$$i = \sum_{k=1}^{\infty} i_k b^{k-1}, i_k \in \{0, 1, \dots, b - 1\} \longrightarrow \phi_b(i) = \sum_{k=1}^{\infty} \frac{i_k}{b^k}.$$

Let $q_1, q_2, \dots, q_s$ be the s first primes. The s-dimensional Halton sequence is

$$H(q_1, q_2, \dots, q_s) = \{\phi_{q_1}(i), \phi_{q_2}(i), \dots, \phi_{q_s}(i)\}_{i=0}^{\infty}.$$

The choice of the primes is crucial, and in the context of this paper only two have to be chosen. The effect of this selection is shown in Fig. 4, where the local structures of two sequences are compared. As can be seen from the definition of the Halton sequences, in 2D the points populate the unit square $[0, 1]^2$ and have to be mapped to the actual computational domain. The process does not take into account the sizes of the holes and therefore we filter the sequence so that the distance between any two points in the final sequence are not closer than $2.5R$, where R is the hole coverage calibrated radius of the holes. The filtered sequences are denoted by $H_F(\cdot, \cdot)$.

Another process is to take a regular pattern and perturb it while avoiding coalescing holes. The perturbations can either be shifts of the underlying patterns or pointwise pseudo-random translations. Since the domains we are interested in are periodic in the angular direction, we only consider pointwise translations in the numerical experiments below.

We do not attempt to define averaging ligament efficiencies for pseudo-random penetration patterns. However, a useful concept used to relate different kinds of patterns is the cell size ϵ, which is the size of the cell containing exactly one hole on average. In the case of a regular $n \times n$-grid on a shell of revolution over $(x, y) \in [-\pi, \pi] \times [0, 2\pi]$, we have $\epsilon = 2\pi/n$. In the limit as $\epsilon \to 0$, we expect regular and quasi-regular penetration patterns to converge.

2.3. hp-FEM

All the numerical simulation reported here are computed with two different high-order continuous Galerkin codes in 2D solving the variational formulation (12) on conforming meshes of triangular and quadrilateral elements. The first one is implemented with Mathematica, providing exact geometry handling of the holes via blending functions [17]. This code has been used to compute smaller examples and in calibration of the second solver.

(a) $H_F(7, 61) \sim 14 \times 14$ (b) $H_F(3, 49) \sim 15 \times 15$
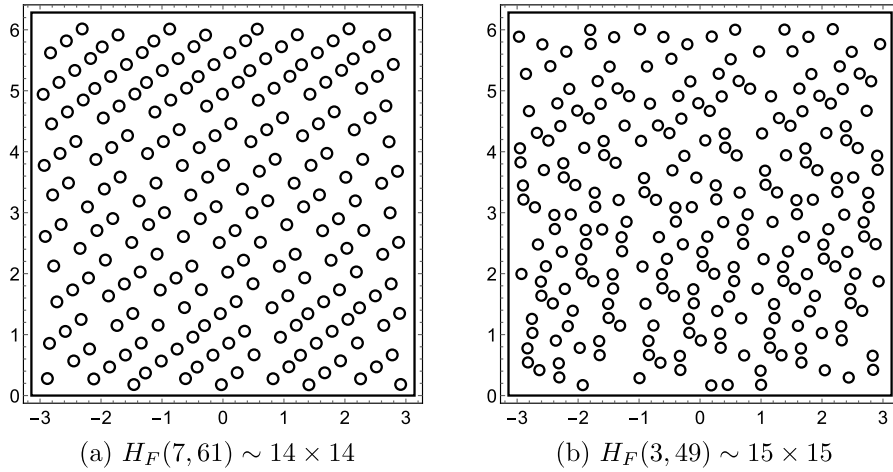
Fig. 4. Filtered quasi-random penetration patterns of Halton type; $H_F(\cdot, \cdot)$. The sequences have been selected by trial and error.

(a) 7×7: hp-mesh.   (b) Detail around one hole.
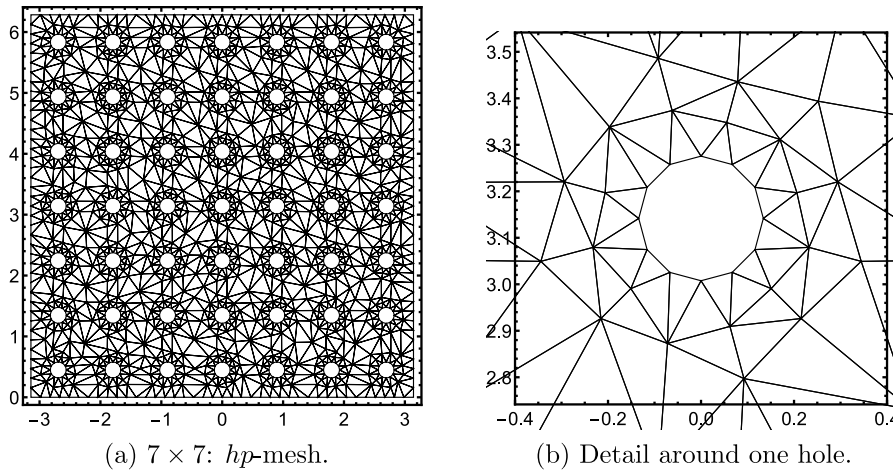
Fig. 5. Typical mesh configuration. In the detail, the hole is programmatically mapped to be circular in the assembly of the system. In the simulations the boundaries at $x_1 = \pm\pi$ are clamped, holes are free, and $x_2 = 0$ and $x_2 = 2\pi$ are periodic.

The second one is a parallel code implemented in FORTRAN90 and MPI. The code allows for any order of polynomials to be used in the elements. Different order of polynomials can be used in different elements in the same mesh. To minimise integration errors on complicated domains, the shape of the elements is represented using the transfinite interpolation method [18] which allows for the edges of the elements to be bent exactly to match the shape of the holes. Together with high order quadrature rules, the integration errors in the discrete problem are controlled. One sample configuration is shown in Fig. 5.

The solution of the eigenvalue problems are computed using ARPACK [19] and MUMPS [20–22] as linear solver called from inside ARPACK. To reduce the computational time and exploit parallelism of modern HPC machines, MPI is used in the assembly of the linear system and in MUMPS to approximate the eigenpairs.

Due to this two-pronged simulation strategy including adaptivity, we have high confidence in the accuracy of the computed results and the conclusions drawn from them.

3. Shell eigenproblem: Eigenmode asymptotics

The free vibration problem for a dimensionally reduced shell in the case of a shell of revolution with constant thickness t leads to the following eigenvalue problem: Find $\mathbf{u}(t)$ and $\omega^2(t) \in \mathbb{R}$ such that

$$\begin{cases} t\,\mathbf{A}_M \mathbf{u}(t) + t\,\mathbf{A}_S \mathbf{u}(t) + t^3\,\mathbf{A}_B \mathbf{u}(t) = \omega^2(t)\,\mathbf{M}(t)\,\mathbf{u}(t) \\ + \text{ boundary conditions.} \end{cases} \tag{11}$$

$\mathbf{u}(t)$ represents the shell displacement field, while $\omega^2(t)$ represents the square of the eigenfrequency. The differential operators $\mathbf{A}_M$, $\mathbf{A}_S$ and $\mathbf{A}_B$ defined above, account for membrane, shear, and bending potential energies, respectively, and are *independent of* t. Finally, $\mathbf{M}(t)$ is the inertia operator, which in this case can be split into the sum $\mathbf{M}(t) = t\, M^l + t^3\, M^r$, with M^l (displacements) and M^r (rotations) *independent of* t.

Let us next consider the variational formulation of problem (11). Accordingly, we introduce the space V of admissible displacements, and consider the problem: Find $(\mathbf{u}(t), \omega^2(t)) \in V \times \mathbb{R}$ such that

$$t\, \mathbf{A_M}(\mathbf{u}(t), \mathbf{v}(t)) + t\, \mathbf{A}_S(\mathbf{u}(t), \mathbf{v}(t)) + t^3\, \mathbf{A}_B(\mathbf{u}(t), \mathbf{v}(t)) =$$
$$\omega^2(t)\, \mathbf{M}(t; \mathbf{u}(t), \mathbf{v}(t)) \quad \forall \mathbf{v} \in V, \tag{12}$$

where $\mathbf{A_M}(\cdot, \cdot)$, $\mathbf{A}_S(\cdot, \cdot)$, $\mathbf{A}_B(\cdot, \cdot)$ and $\mathbf{M}(t; \cdot, \cdot)$ are the bilinear forms associated with the operators $\mathbf{A}_M$, $\mathbf{A}_S$, $\mathbf{A}_B$ and $\mathbf{M}(t)$, respectively. Obviously, the space V and the three bilinear forms depend on the chosen shell model, here the mathematical shell model.

3.1. Symmetries

In the standard (non-perforated) case the model for a shell of revolution can be further reduced to a one-dimensional one, since the eigenmode must be periodic in the angular direction. Assuming that the transverse deflection $w(x) \neq 0$, it follows from the strains that the eigenmode $\mathbf{u}(x, y)$ has either one of the forms

$$\mathbf{u}_1(x, y) = \begin{pmatrix} u(x)\cos(ky) \\ v(x)\sin(ky) \\ w(x)\cos(ky) \\ \theta(x)\cos(ky) \\ \psi(x)\sin(ky) \end{pmatrix} \text{ or } \mathbf{u}_2(x, y) = \begin{pmatrix} u(x)\sin(ky) \\ v(x)\cos(ky) \\ w(x)\sin(ky) \\ \theta(x)\sin(ky) \\ \psi(x)\cos(ky) \end{pmatrix}. \tag{13}$$

In other words, the selection of the ansatz in the angular direction is not unique. Hence, the corresponding eigenvalues are in fact always double eigenvalues, unless the mode is a torsion mode, i.e., one acting in the tangent plane of the surface. For torsion modes the transverse deflection is identically zero, $w(x) = 0$.

3.2. Asymptotics of parabolic shell eigenmodes

Parameter-dependent deterministic asymptotics (asymptotics as $t \to 0$) of the smallest eigenpairs are known rigorously for parabolic and elliptic shells, and well-understood for hyperbolic ones.

First, let us for simplicity consider just one component of the displacement field. The transverse profile w of the smallest eigenmode has a parabolic profile, see [7]. This means that we can omit torsional modes from our discussion here. Shells exhibit a rich variety of boundary layers, including internal layers, each of which has its own characteristic length. Indeed, every shell eigenmode can be viewed as a linear combination of characteristic features. Formally, we can write for w, $(x, y) \in D$:

$$w(x, y) = \sum_k w^{(k)}(x, y),$$

where each $w^{(k)}(x, y)$ has its own parameter-dependent characteristic length, with the smooth part with length scale equal to the diameter of the domain D. In [7] it is also established that for the smallest eigenmode the boundary layers do not carry significant amount of energy and we can restrict our discussion to the smooth part only. This has the consequence that the natural choice for a basis − the Fourier basis the functions of type

$$w_{mn}(x, y) = \cos\left(\frac{m}{2}x\right)\cos(ny), \quad x \in [-\pi, \pi], \quad y \in [0, 2\pi], \tag{14}$$

where $m, n \in \mathbb{Z}$, leading to general eigenbasis

$$W = \{w_{mn}(x, y)\}_{m,n=0}^{\infty},$$

does not satisfy the axial boundary conditions. As is demonstrated below, this is indeed a sufficient model for our purposes. Similar expansions for different components can be derived with axial parts

$$u(x) = \sin\left(\frac{m}{2}x\right), v(x) = \cos\left(\frac{m}{2}x\right), \theta(x) = \sin\left(\frac{m}{2}x\right), \psi(x) = \cos\left(\frac{m}{2}x\right)$$

and angular parts depending on the chosen ansatz.

Notice, that we can now track modes in the parameter space using wavenumbers m and n only, since for every component of the eigenmode they are the same even if the trigonometric basis function may differ. Hence, we can use notation $(\lambda_{mn}, \mathbf{u}_{mn})$ for a corresponding eigenpair.

For a fixed value of t the eigenvalues can be ordered

$$\lambda_{\min}(t) = \lambda_{m_1 n_1}(t) \leq \lambda_{m_2 n_2}(t) \leq \cdots \leq \lambda_{m_j n_j}(t) \leq \cdots$$
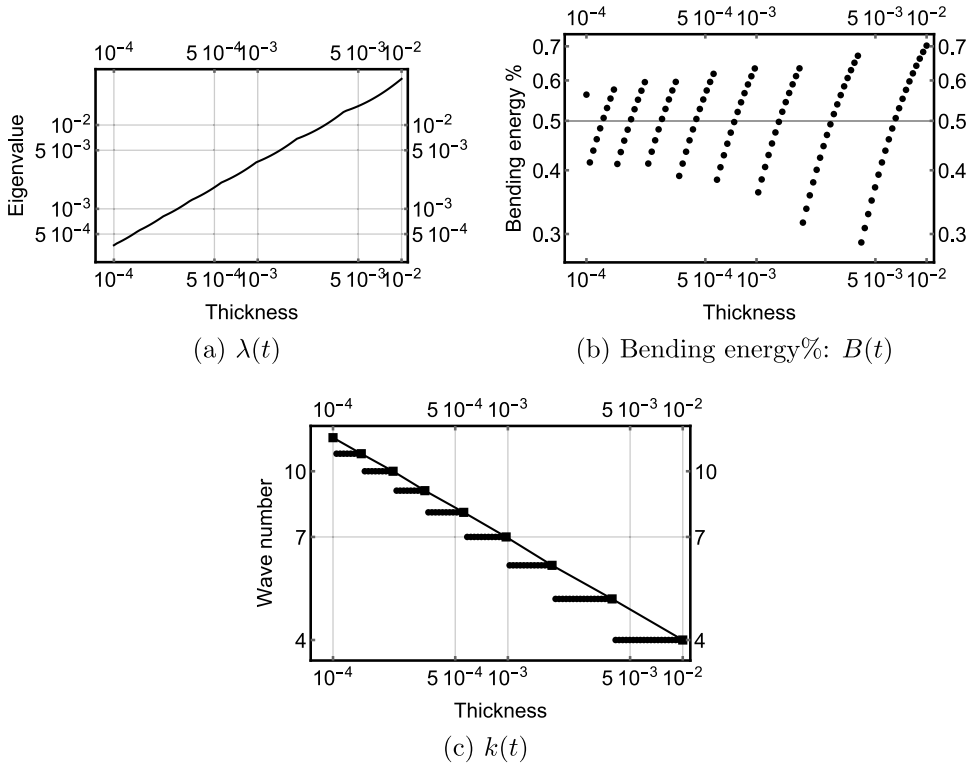
Fig. 6. Reference asymptotic analysis: $t \in [10^{-4}, 10^{-2}]$, uniform logarithmic scale with 100 samples. Observed rates: $\lambda(t) \sim t$; $k(t) \sim t^{-1/4}$; $B(t) \to 1/2$.

and naturally this is an ordering of the eigenmodes as well. Here $m_1 = 1$ always, i.e., the smallest eigenpair is of type

$$(\lambda_{1n_i}(t), \mathbf{u}_{1n_i}(t))$$

with $n_i \geq 1$.

For parabolic shells, the asymptotics of the eigenvalues and the angular wave number k are known and are summarised in Theorem 1. These results are also visualised in Fig. 6.

Theorem 1 ([7,8]). *For cylindrical shells of revolution, the smallest eigenvalue $\lambda_{\min}(t)$ and the integer valued wavenumber*

$$k_{\min}(t) := \min\{k \in \mathbb{N} \mid \lambda_{\min}(t) = \lambda_{1k}(t)\}$$

scale as functions of dimensionless thickness t:

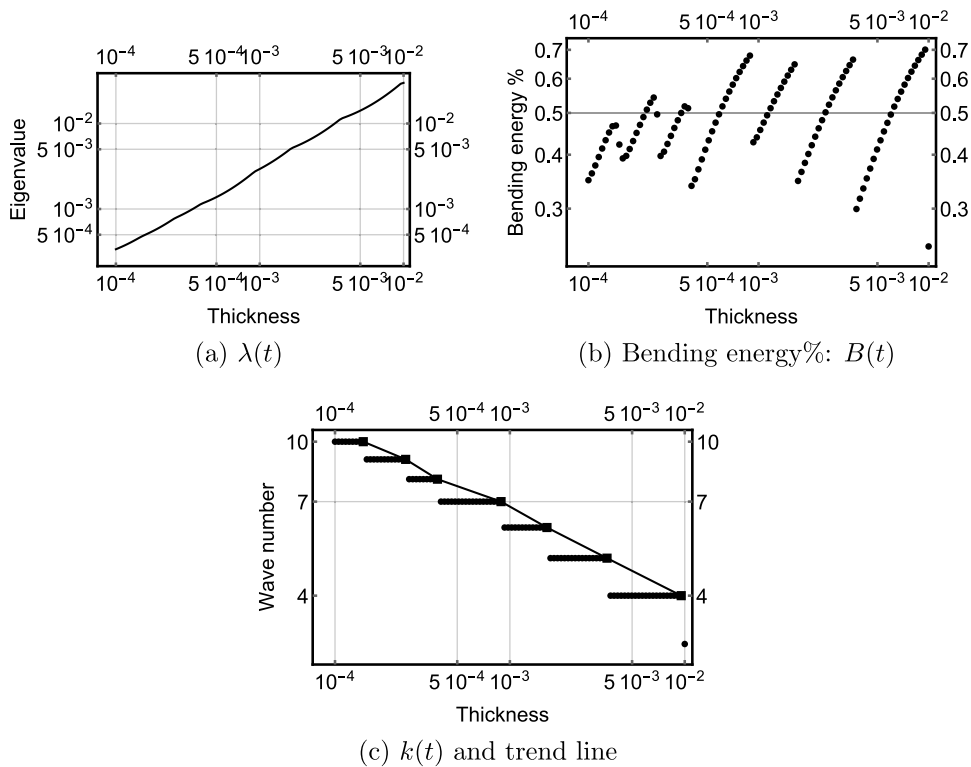$$\lambda_{\min}(t) \sim t, \quad k_{\min}(t) \sim t^{-1/4}.$$

As $t \to 0$, the ratio of the bending energy over the total energy $B(t) \to 1/2$.

The bending energy convergence graph is of particular interest (Fig. 6b). The convergence is somewhat unusual — the ratio of the bending energy converges to a limit of 1/2, but for parabolic shells, the relative amount of the bending energy in the smallest mode decreases as long as its angular wave number remains constant. Therefore, one has to observe the behaviour of the averages within the bands.

3.3. A priori model for asymptotics of perforated parabolic shell eigenmodes

It is clear that the perforations will have an effect on the asymptotics of the smallest mode. In standard homogenisation theory the idea is to let the hole coverage and the dimensionless thickness tend to zero simultaneously. Our approach is different, however. We keep the hole coverage percentage fixed, and let the number of holes increase and thereby let the sizes of the holes decrease.

Consider a regular $g \times g$ perforation pattern ($g \in \mathbb{N}$) or alternatively a given cell size ϵ in the language of homogenisation ($\epsilon \in \mathbb{R}$). As the thickness t changes, so does the angular wave number k. Let us assume that g is even. If $k = g/2$, the ansatz (13) does not produce double eigenvalues, since the two candidate modes have their maximal amplitudes either

(a) $\lambda(t)$

(b) Bending energy%: $B(t)$

(c) $k(t)$ and trend line

Fig. 7. Asymptotic analysis: 14×14 regular grid; hole coverage 12%; $t \in [10^{-4}, 10^{-2}]$, uniform logarithmic scale with 100 samples. Observed rates: $\lambda(t) \sim t$; $k(t) \sim t^{-1/4}$, $k(t) \le 7$. Notice the width of the interval of thicknesses at $k = 7$. Behaviour of $B(t)$ changes at $k = 7$.

at the holes or on the domain in between. This leads to separation within the cluster. Let us denote the corresponding wave number and thickness, as k_c and t_c, respectively. If $t \le t_c$ and thus $k \ge k_c$, the smallest mode acts more on the holes which are "softer" and the wave number k cannot grow as fast as in the non-perforated configuration as $t \to 0$.

In Figs. 7–9 we show three sets of results on different regular grids. Somewhat surprisingly, the eigenvalue asymptotics remain as in the standard case. However, as predicted, the angular wave number follows the standard asymptotics only down to the critical thickness, below which the trend falls behind. The trend lines are computed by collecting the first thickness of the observed k-value. For the 30×30 regular grid the critical thickness is below the range of thicknesses considered and the asymptotics are exactly those of the standard case.

The observed bending energy ratios tell the same story. As the local features start to have stronger relative effects, the predicted energy balances cannot hold below the critical thickness.

We can now predict the asymptotic behaviour of the perforated parabolic shells of revolution using the existing theory as foundation.

Conjecture 1 (*Asymptotics of Perforated Parabolic Shells of Revolution*). *Given a $g \times g$ regular perforation pattern, there exists a critical dimensionless thickness t_c at which the angular wave number $k_c \approx g/2$. For thicknesses $t < t_c$ the asymptotics of the smallest eigenmode do not conform to those of the non-perforated case.*

4. Dynamics of clusters of modes

In this section we discuss another feature of parameter-dependent eigenproblems, the dynamics of the modes. In the context of shells of revolution it is more accurate to refer to clusters of modes as we have already established above. The asymptotics indicate that the smallest mode changes as the parameter $t \to 0$. This observation raises an interesting question: What is the ordering of the modes at the given value of the parameter and how does the relative ordering change as the parameter changes? The correct approach is to consider the modes as a dynamical system with the thickness as the parameter.

4.1. Dynamics of shell eigenmodes

Using the Fourier expansion idea outlined in Section 3.2 above, every mode can be identified using angular and axial wave numbers. By computing the spectrum and then identifying the modes, we can track the relative orderings of the

(a) $\lambda(t)$

(b) Bending energy%: $B(t)$

(c) $k(t)$ and trend line
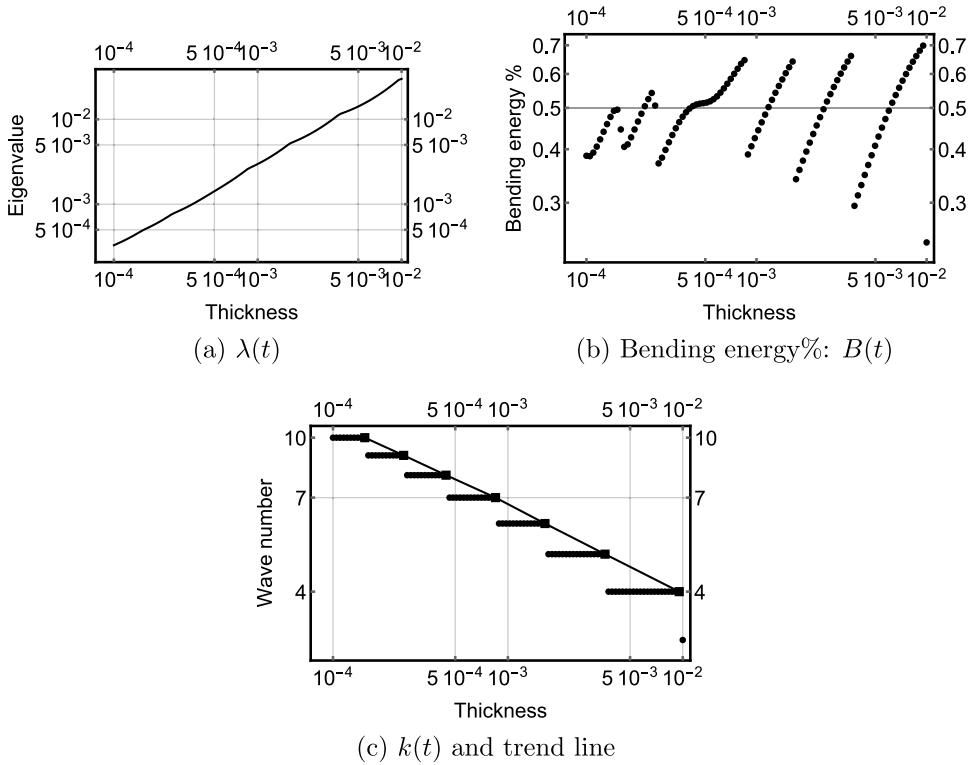
Fig. 8. Asymptotic analysis: 15×15 regular grid; hole coverage 12%; $t \in [10^{-4}, 10^{-2}]$, uniform logarithmic scale with 100 samples. Observed rates: $\lambda(t) \sim t$; $k(t) \sim t^{-1/4}$, $k(t) \leq 7$. Notice that the width of the interval of thicknesses at $k = 7$ extends below $t = 5 \times 10^{-4}$. Again, behaviour of $B(t)$ changes at $k = 7$.

modes as the parameter changes. In Fig. 10 three different regular grids are considered. In each case every mode which eventually becomes the smallest one is traced through the sampled parameter values. As one would expect based on the observation on the asymptotics, it should not come as a surprise that at the critical thickness t_c the dynamics change as well. For instance, consider the two modes $k = 6$ and $k = 7$, indicated with red and purple lines, respectively. Their relative positions in the spectrum change roughly at the same rate until the critical thickness is reached in the coarser perforations. In the reference case, the mode $k = 6$ is not among the 40 smallest modes at the lower limit of the interval, whereas in the 14×14-case it is still within that range.

### 4.2. A priori model for perforated shell dynamics

Following the discussion in Section 3.3 we can now formulate a similar conjecture for the dynamics.

Conjecture 2 (*Dynamics of Perforated Parabolic Shells of Revolution*). *Given a $g \times g$ regular perforation pattern, there exists a critical dimensionless thickness t_c at which the angular wave number $k_c \approx g/2$. For thicknesses $t < t_c$ the dynamics of the eigenmodes do not conform to those of the non-perforated case. For thicknesses $t < t_c$ the mixing of modes happens at a lower rate.*

5. Numerical experiments

In this section we consider a series of regular perforation patterns and one filtered Halton or Quasi-Monte Carlo pattern. The numerical experiments are designed to demonstrate the features outlined above in configurations where the dimensionless thicknesses are within the practical range.

As before, we consider three different hole coverage percentages: 7, 12, and 25%. The discussion above suggests that the bending energy ratio $B(t)$ is a sensitive indicator of local features in the smallest eigenmodes. It should be noted, however, that the limit $\lim_{t \to 0} B(t)$ of course depends on the hole coverage percentage. As can be seen below, it is sufficient to observe local changes in the convergence of $B(t)$ rather than focus on the limit value.

(a) $\lambda(t)$

(b) Bending energy%: $B(t)$

(c) $k(t)$ and trend line
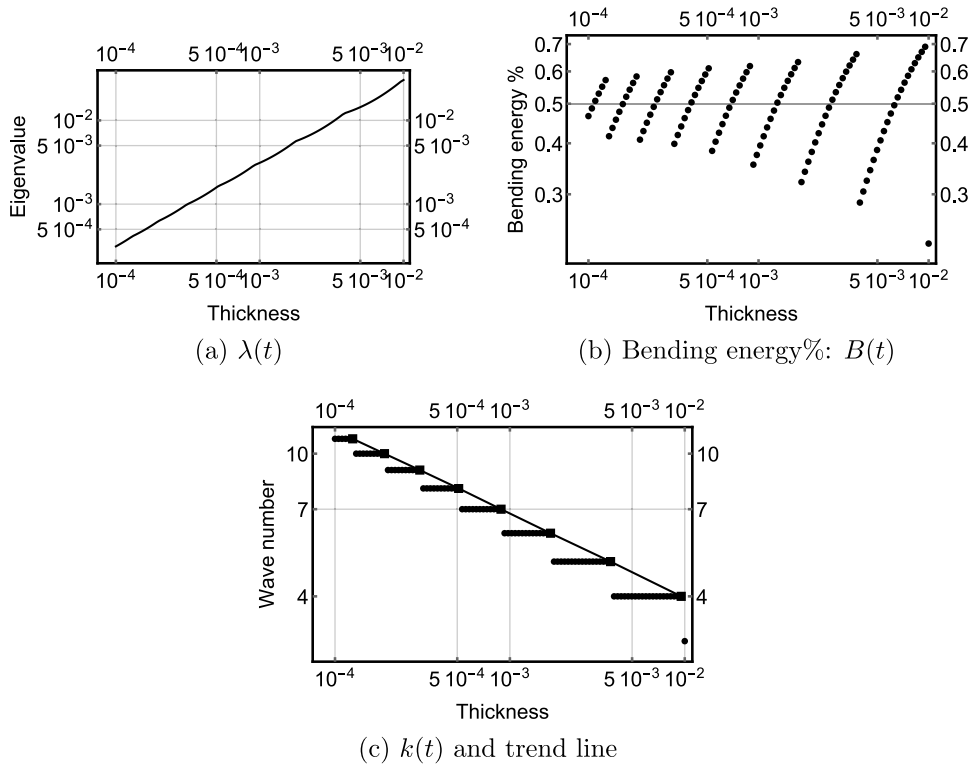
Fig. 9. Asymptotic analysis: 30 × 30 regular grid; hole coverage 12%; $t \in [10^{-4}, 10^{-2}]$, uniform logarithmic scale with 100 samples. Observed rates: $\lambda(t) \sim t$; $k(t) \sim t^{-1/4}$. Notice that the width of the interval of thicknesses at $k = 7$ does not extend below $t = 5 \times 10^{-4}$. Within the parameter range $B(t) \to 1/2$.


(a) 14 × 14

(b) 15 × 15

(c) Reference and 30 × 30
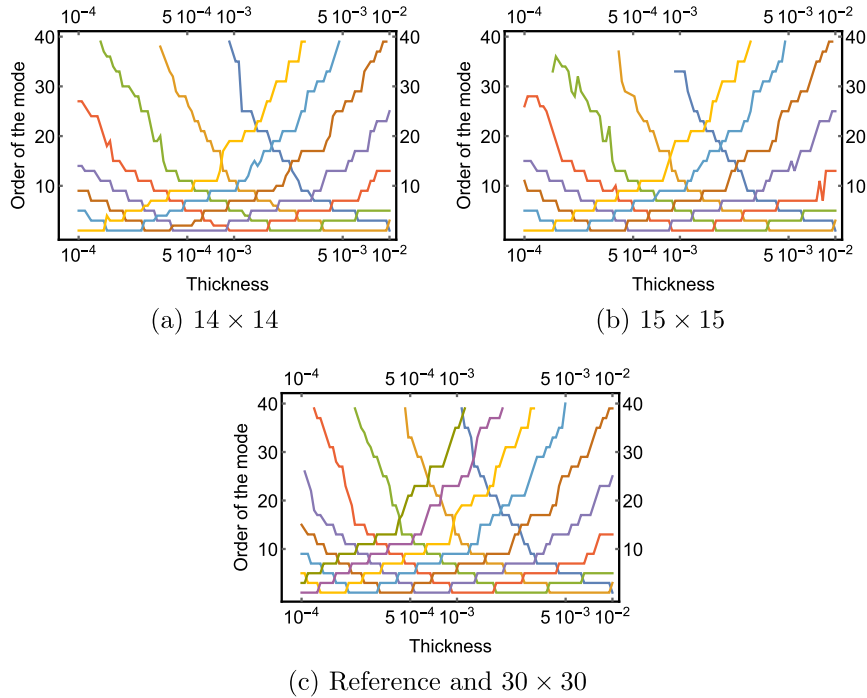
Fig. 10. Relative ordering of modes: loglinear plot; hole coverage 12%; $t \in [10^{-4}, 10^{-2}]$, uniform logarithmic scale with 100 samples. Different colours refer to different eigenmodes and their relative positions in the spectrum. The bottom line in each plot indicates the smallest mode the value of which can be inferred from Figs. 7–9. The upper sections of the figures appear sparser, since only those modes that ever become the smallest ones are shown. (For interpretation of the references to colour in this figure legend, the reader is referred to the web version of this article.)
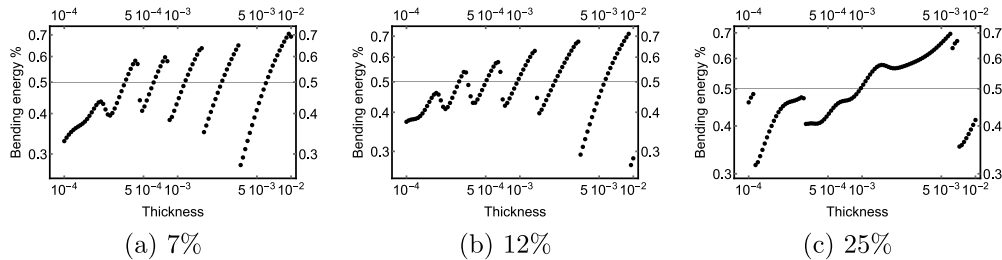
Table 1

Observed rates for $\lambda(t)$ and $k(t)$, over a set of perforations; $t \in [10^{-4}, 10^{-2}]$, uniform logarithmic scale with 100 samples. $H_F(7, 61) \sim 14 \times 14$. Rates for $k(t)$ have been computed over the interval $k_1 \leq k(t) \leq k_2$.

QoI	%	7×7	8×8	10×10	12×12	$H_F(7, 61)$
$\lambda(t)$	7	0.93	0.96	0.98	0.99	1.01
	12	0.97	0.98	1.00	1.00	1.02
	25	0.99	1.02	1.10	1.10	1.09
$[k_1, k_2]$		$[4, 7]$	$[5, 8]$	$[6, 10]$	$[4, 6]$	$[4, 7]$
$k(t)$	7	0.21	0.20	0.23	0.24	0.23
	12	0.22	0.21	0.22	0.24	0.23
	25	0.24	0.24	0.25	0.22	0.21

(a) 12×12, $4 \leq k(t) \leq 6$

(b) $H_F(7, 61)$, $4 \leq k(t) \leq 7$
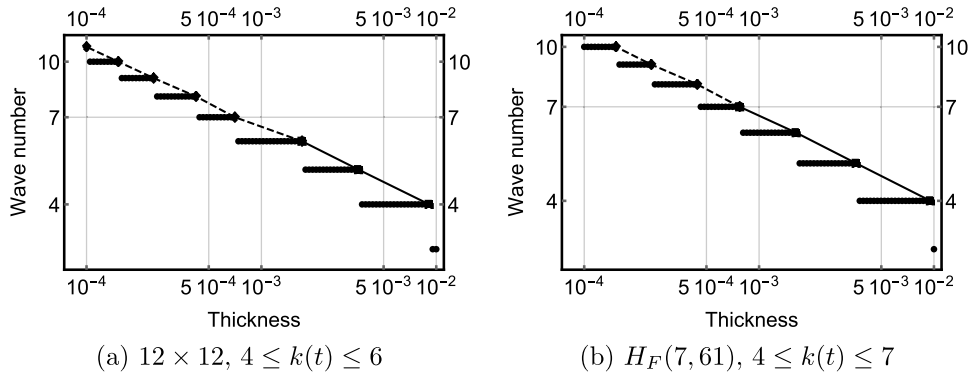
Fig. 11. Asymptotic analysis: $k(t)$ and trend line; hole coverage 12%; $t \in [10^{-4}, 10^{-2}]$, uniform logarithmic scale with 100 samples. The rate in Table 1 is computed in the interval indicated with a solid line and in the caption, dashed line represents the perturbed part.
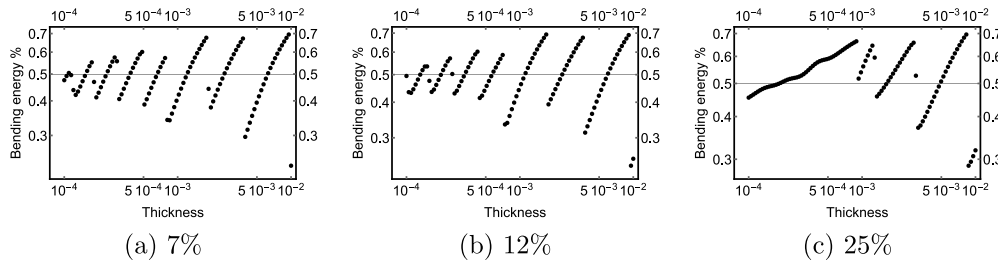

(a) 7%

(b) 12%

(c) 25%

Fig. 12. Asymptotic analysis: Regular 8×8 grid; $t \in [10^{-4}, 10^{-2}]$, uniform logarithmic scale with 100 samples. Hole coverage percentages are indicated in the subtitles.

5.1. Regular perforations

Let us consider our standard cylinder with four different regular perforations. As shown in Fig. 6 the range of angular wave numbers is $[4, 12]$. Therefore each grid in the set $G = \{g \times g \mid g \in \{7, 8, 10, 12\}\}$ should exhibit some local features. The computed rates for $\lambda(t)$ and $k(t)$ are given in Table 1. Interestingly, the eigenvalues decay asymptotically as in the standard case. For the wave numbers, the situation is more complicated. In each case, we can identify a range of wave numbers within which the asymptotic growth rate is close to that in the standard case. In Fig. 11 two cases are shown where asymptotic and local ranges are indicated. The connection between the $B(t)$ and the size of the grid g is evident in Figs. 12 and 13. For $g = 8$ the energy band corresponding to $k(t) = 4$ stands apart, and similarly for the pair $g = 12$ and $k(t) = 6$. For 25% hole coverage, the onset of local features appears as the loss of clear band structure at the critical $k(t)$.

5.2. Quasi Monte-Carlo perforations

We have included in the set of grids one filtered Halton grid, $H_F(7, 61)$. We have included the rate data in Table 1 and the energy bands in Fig. 14. Since $H_F(7, 61) \sim 14 \times 14$ these results should be compared with those of Fig. 7. Even though at 12% the local features do emerge at around $k(t) = 7$, the transition is not as sharp. Since the modes in the smallest cluster are not maximally separated due to irregularity of the pattern, this is in line with our discussion in the previous sections.

Fig. 13. Asymptotic analysis: Regular 12 × 12 grid; $t \in [10^{-4}, 10^{-2}]$, uniform logarithmic scale with 100 samples. Hole coverage percentages are indicated in the subtitles.
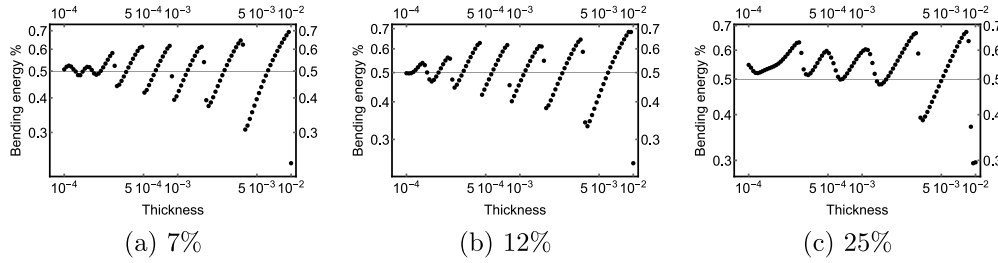
Fig. 14. Asymptotic analysis: Filtered Halton grid; $H_F(7, 61) \sim 14 \times 14$; $t \in [10^{-4}, 10^{-2}]$, uniform logarithmic scale with 100 samples. Hole coverage percentages are indicated in the subtitles.
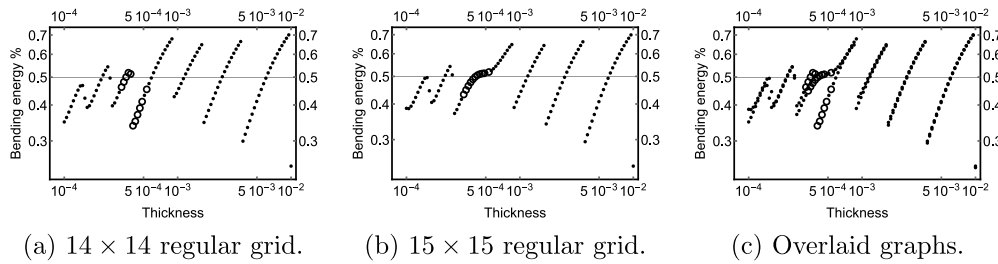
Fig. 15. Transition analysis: Comparison of cluster separation measured by energy; Hole coverage percentage is 12%; $t \in [10^{-4}, 10^{-2}]$, uniform logarithmic scale with 100 samples. Clusters within which the bending ratios differ by more than 1% are indicated with open circles.

5.3. Analysis of transition from global to local features

Already in Fig. 1 we have seen how in the neighbourhood of the critical thickness t_c the smallest cluster can be separated when the grid parameter g is even. However, also in the case of g odd (see Fig. 8) such a transition appears to take place, but not as sharply.

In Fig. 15 the same data already shown above for the regular grid cases of 14 × 14 and 15 × 15 is augmented by indicating the clusters where the two modes of the cluster have a difference in their bending energy ratios $B(t)$. The chosen tolerance is 1%. We observe, that as expected the transition zone or parameter interval is the same. The only difference is in the sharpness of the transition.

Within the transition interval it can happen that due to the separation of the smallest cluster the second smallest "slides" in between the two separated modes. (This is visible already in Fig. 1.) This phenomenon is the reason why in mode identification the modes belonging to the same cluster can appear in non-adjacent positions.

6. Conclusions

Parameter-dependent eigenproblems on perforated domains are intricate. Through computational means one can gain insight into the complex interplay of the parameter-dependent features of the modes and the perforation patterns. Our model problem, free vibration of thin perforated parabolic shells of revolution, is rich in interesting features which can be analysed and in some cases predicted based on the existing a priori knowledge of such problems.

The key observation here is the connection between the value of the parameter and the perforation density. For every perforation pattern there exists a critical value of the parameter which divides the parameter range into two parts where

either the global or local features of the smallest eigenmodes dominate. For a regular $g \times g$-perforation pattern, the critical thickness is reached when the lowest mode has an angular wave number $k \sim g/2$. For instance, for parabolic shells considered here, the asymptotic connection between the wavenumber and the dimensionless thickness is $k(t) \sim t^{1/4}$. This observation is supported both by geometric arguments and numerical experiments. This is likely to be of significance when effective material parameters are searched for via homogenisation in practical engineering applications.

References

[1] H. Martikka, E. Taitokari, Design of perforated shell dryings drums, Mech. Eng. Res. (2012).

[2] A.L. Kalamkarov, I.V. Andrianov, D. Weichert, Asymptotic analysis of perforated shallow shells, Internat. J. Engrg. Sci. 53 (2012) 1–18.

[3] M.J. Jhung, S.O. Yu, Study on modal characteristics of perforated shell using effective Young's modulus, Nucl. Eng. Des. (2011).

[4] J. Torabi, R. Ansari, A higher-order isoparametric superelement for free vibration analysis of functionally graded shells of revolution, Thin-Walled Struct. 133 (2018) 169–179.

[5] R. Ansari, E. Hasrati, J. Torabi, Vibration analysis of pressurized sandwich FG-CNTRC cylindrical shells based on the higher-order shear deformation theory, Mater. Res. Express 6 (4) (2019) 045049.

[6] Ö. Civalek, Numerical analysis of free vibrations of laminated composite conical and cylindrical shells: Discrete singular convolution (DSC) approach, J. Comput. Appl. Math. 205 (1) (2007) 251–271.

[7] L. Beirão da Veiga, H. Hakula, J. Pitkäranta, Asymptotic and numerical analysis of the eigenvalue problem for a clamped cylindrical shell, Math. Models Methods Appl. Sci. (M3AS) 18 (11) (2008) 1983–2002.

[8] E. Artioli, L. Beirão da Veiga, H. Hakula, C. Lovadina, Free vibrations for some koiter shells of revolution, Appl. Math. Lett. 21 (12) (2008) 1245–1248.

[9] E. Artioli, L. Beirão da Veiga, H. Hakula, C. Lovadina, On the asymptotic behaviour of shells of revolution in free vibration, Comput. Mech. 44 (1) (2009) 45–60.

[10] M. Chaussade-Beaudouin, M. Dauge, E. Faou, Z. Yosibash, High frequency oscillations of first eigenmodes in axisymmetric shells as the thickness tends to zero, in: Recent Trends in Operator Theory and Partial Differential Equations, Springer International Publishing, 2017, pp. 89–110.

[11] M. Chaussade-Beaudouin, M. Dauge, E. Faou, Z. Yosibash, Free vibrations of axisymmetric shells: Parabolic and elliptic cases, Asymptot. Anal. 104 (2017) 1–47.

[12] M. Malinen, On the classical shell model underlying bilinear degenerated shell finite elements: general shell geometry, Internat. J. Numer. Methods Engrg. 55 (6) (2002) 629–652.

[13] J. Pitkäranta, A.-M. Matache, C. Schwab, Fourier mode analysis of layers in shallow shell deformations., Comput. Methods Appl. Mech. Engrg. 190 (2001) 2943–2975.

[14] M. Forskitt, J.R. Moon, P.A. Brook, Elastic properties of plates perforated by elliptical holes, Appl. Math. Model. (1991).

[15] K. Burgemeister, C. Hansen, Calculating resonance frequencies of perforated panels, J. Sound Vib. 196 (4) (1996) 387–399.

[16] J.H. Halton, Algorithm 247: Radical-inverse quasi-random point sequence, Commun. ACM 7 (12) (1964) 701–702.

[17] H. Hakula, T. Tuominen, Mathematica implementation of the high order finite element method applied to eigenproblems, Computing 95 (1) (2013) 277–301.

[18] P. Solin, K. Segeth, I. Dolezel, Higher Order Finite Element Methods, Har/Cdr, Chapman and Hall/CRC, 2003.

[19] R. Lehoucq, D. Sorensen, C. Yang, ARPACK users' guide: Solution of large-scale eigenvalue problems with implicitly restarted arnoldi methods, in: Software, Environments, Tools, Society for Industrial and Applied Mathematics, 1998.

[20] P.R. Amestoy, I.S. Duff, J.-Y. L'Excellent, Multifrontal parallel distributed symmetric and unsymmetric solvers, Comput. Methods Appl. Mech. Engrg. 184 (2000) 501–520.

[21] P.R. Amestoy, I.S. Duff, J. Koster, J.-Y. L'Excellent, A fully asynchronous multifrontal solver using distributed dynamic scheduling, SIAM J. Matrix Anal. Appl. 23 (2001) 15–41.

[22] P.R. Amestoy, A. Guermouche, J.-Y. L'Excellent, S. Pralet, Hybrid scheduling for the parallel solution of linear systems, Parallel Comput. 32 (2006) 136–156.